Interband second-order nonlinear optical susceptibility of asymmetric coupled quantum wells ⊘

Rithvik Ramesh ✉ ⓘ ; Teddy Hsieh ⓘ ; Alec M. Skipper ⓘ ; Qian Meng ⓘ ; Kevin C. Wen ⓘ ;
Farbod Shafiei ⓘ ; Mark A. Wistey ⓘ ; Michael C. Downer ⓘ ; Jacob B. Khurgin ⓘ ; Seth R. Bank ⓘ

Check for updates

View Online   Export Citation   CrossMark

Interband second-order nonlinear optical susceptibility of asymmetric coupled quantum wells

View Online   Export Citation   CrossMark

Rithvik Ramesh,[1,a] (iD) Teddy Hsieh,[1] (iD) Alec M. Skipper,[1] (iD) Qian Meng,[1] (iD) Kevin C. Wen,[1] (iD) Farbod Shafiei,[2] (iD)
Mark A. Wistey,[3] (iD) Michael C. Downer,[2] (iD) Jacob B. Khurgin,[4] (iD) and Seth R. Bank[1] (iD)

AFFILIATIONS

[1]Microelectronics Research Center and the Electrical and Computer Engineering Department, The University of Texas at Austin,
 Austin, Texas 78758, USA
[2]Physics Department, The University of Texas at Austin, Austin, Texas 78758, USA
[3]Physics Department, Texas State University, San Marcos, Texas 78666, USA
[4]Department of Electrical and Computer Engineering, Johns Hopkins University, Baltimore, Maryland 21218, USA

[a]Author to whom correspondence should be addressed: rithvikr@utexas.edu

ABSTRACT

Asymmetric molecular bonds possess a microscopic second-order nonlinear optical polarizability $\boldsymbol{p}^{(2)}$. Crystals built from them possess a macroscopic second-order nonlinear optical susceptibility, $\chi^{(2)}$, if their structure lacks centrosymmetry. $\chi^{(2)}$ can be enhanced by introducing additional asymmetry at the meta-structural level. Here, we use a dipole matrix formalism to calculate $\chi^{(2)}$ of asymmetric GaAs/AlGaAs coupled quantum well structures at telecommunication frequencies, for which interband (rather than previously considered intersubband) optical transitions govern optical nonlinearities. Using unit cell and envelope wavefunctions and considering all possible transitions between two bound electron and two bound hole states, we predict tenfold enhancement in $\chi^{(2)}$ in previously underexplored ranges of quantum well asymmetry and coupling barrier thickness. This work paves the way toward enhanced, tailorable second-order optical nonlinearities for semiconductor digital alloy and superlattice structures.

Published under an exclusive license by AIP Publishing. https://doi.org/10.1063/5.0168596

Nonlinear optical processes are becoming increasingly important for applications in optical communications,[1] information processing,[2] quantum photonics,[3] optical frequency combs,[4] integrated photonics,[5] and laser design.[6] Second-order optical nonlinearities are advantageous because they require significantly lower light intensities than third-order nonlinearities, yet bulk second-order nonlinearity is only present in non-centrosymmetric crystals.[7] Even when using centrosymmetric materials, it is possible to engineer second-order nonlinearity through structures that break inversion symmetry.[8] Traditional second-order nonlinear optical materials, such as LiNbO$_3$, have relatively strong bulk second-order susceptibility, $\chi^{(2)}$, and can be grown with high quality.[9] While such complex oxides can have strong nonlinearities and large transparency windows, they are generally difficult to integrate with semiconductor substrates, making it difficult to use the complex oxides with silicon photonics or semiconductor photonics platforms. As a result, there is significant interest in developing a semiconductor material platform with large and tailorable $\chi^{(2)}$.

Semiconductor digital alloys, such as AlInAsSb, are well suited for tailored nonlinearities because the band offsets, bandgaps, and layer thicknesses of the semiconductor heterostructure can be very finely controlled.[10,11] Utilizing resonant enhancement of $\chi^{(2)}$, very strong (on the order of 10 nm/V) intersubband optical nonlinearities in semiconductor structures have been demonstrated for mid to far infrared fundamental wavelengths.[12,13] The operating wavelengths of intersubband transitions are restricted by the conduction band offset. By contrast, interband transitions can leverage the bandgap to achieve strong and tailorable nonlinearities in the near-IR, specifically the optical communication S, C, L, and U bands from 1450 to 1700 nm.[14] Previous studies into interband nonlinearities, however, predicted $\chi^{(2)}$ only on the order of the bulk susceptibility with established quantum well (QW) materials (e.g., AlGaAs/GaAs).[15,16] As a result, interband nonlinearities in semiconductors have remained comparatively underexplored. In this work, calculating $\chi^{(2)}$ from asymmetric coupled QWs with rigorous wavefunctions and including contributions from all

06 January 2024 18:07:03

possible transitions between heavy hole and electron bound states, we predict tenfold enhancement in $\chi^{(2)}$ at near-IR wavelengths. This work identifies the previously unrecognized importance of dipole-like diagonal intersubband matrix elements toward significant interband $\chi^{(2)}$ enhancement. Furthermore, we explore the design degrees of freedom of the asymmetric coupled QW structure, enabling the design of a semiconductor platform with large nonlinearities at technologically important wavelengths.

The strength of each term in the expansion of polarization is characterized by a susceptibility, $\chi^{(n)}$. Using the density matrix formalism, the second-order susceptibility for a multi-QW structure is given by[17]

$$\chi_{ijk}^{(2)}(\omega_1, \omega_2) = \frac{N_z e^3}{2\epsilon_0 \hbar^2} \sum_P \sum_{b_1,b_2,b_3} \sum_{l,m,n} f_{b,l} \sum_{k_\parallel} \frac{\langle \phi_{1,l}^*|r_i|\phi_{2,m}\rangle \langle \phi_{2,m}^*|r_j|\phi_{3,n}\rangle \langle \phi_{3,n}^*|r_k|\phi_{1,l}\rangle}{\left[\omega_{b_2,m}(k_\parallel) - \omega_{b_1,l}(k_\parallel) - \omega_1 - \omega_2\right]\left[\omega_{b_3,n}(k_\parallel) - \omega_{b_1,l}(k_\parallel) - \omega_2\right]}. \tag{1}$$

In Eq. (1), N_z is the number of QWs per unit length, ω_1 and ω_2 are the input photon frequencies, $\omega_{b,m}$ is the frequency of the denoted energy level (l, m, n) in the indicated band $(b_{1,2,3})$ at the given wavevector $k_\parallel$, and [m,n,l] are used to index the energy levels such that the summation over [m,n,l] considers all possible transitions between the first two heavy hole and electron states. The summation over P corresponds to the possible polarization combinations of the input and output photons. The wavefunctions in Eq. (1) can be written in the Bloch formalism to separate the unit cell and envelope portions,

$$\phi_{b,n} e^{ik_\parallel r_\parallel} = u_{b,n}(r) \psi_{b,n}(z) e^{ik_\parallel r_\parallel}. \tag{2}$$

Here, the unit cell portion of the wavefunction is $u_{b,n}(r)$, and the envelope portion is $\psi_{b,n}(z)$, where b and n index the band and state, respectively. For interband nonlinearities near resonance, the transitions occur between the bound states in the conduction band and

valence band that are closest to the band edge. Since heavy hole states lie higher in energy than light hole states, the relevant transitions will occur between heavy hole and electron states.[18] Because this is an interband process, the ground states of the transitions are filled valence states, so the Fermi function of the ground state, $f_{b1,l}$, is unity. Finally, the electric field portion of the radiation is assumed to be polarized along the growth direction, z.[15] It is necessary that a component of the electric field be along the growth direction (perpendicular to the QW planes) to excite the QW enhancement of $\chi^{(2)}$. In experiments, this can be achieved using TE polarized input light at an incidence angle to the surface of the QW sample. TM polarized input would not excite the QW nonlinearity because the electric field oscillates parallel to the QW plane. With these assumptions, including line broadening and separating the envelope and unit cell in the Bloch formalism, $\chi^{(2)}$ simplifies to[15]

$$\chi_{xzx}^{(2)}(\omega_1, \omega_2) = \frac{N_z e^3 r_{e,hh}^2}{6\epsilon_0 \hbar^2} \sum_{k_\parallel} \sum_{m,n} \sum_l \left(\frac{\langle \psi_{hhm}|\psi_{en}\rangle \langle \psi_{en}|z|\psi_{el}\rangle \langle \psi_{el}|\psi_{hhm}\rangle}{\left(\omega_{hhm}^{en}(k_\parallel) - \omega_1 - \omega_2 + i\Gamma\right)\left(\omega_{hhm}^{el}(k_\parallel) - \omega_1 + i\Gamma\right)} \right.$$
$$\left. - \frac{\langle \psi_{en}|\psi_{hhm}\rangle \langle \psi_{hhm}|z|\psi_{hhl}\rangle \langle \psi_{hhl}|\psi_{en}\rangle}{\left(\omega_{hhm}^{en}(k_\parallel) - \omega_1 - \omega_2 + i\Gamma\right)\left(\omega_{hhl}^{en}(k_\parallel) - \omega_1 + i\Gamma\right)} \right). \tag{3}$$

In Eq. (3), ω_{hhi}^{ej} is the frequency of the transition between the denoted conduction and heavy hole states, where $i = m, l$ and $j = n, l$. Detuning was accounted for by assuming a second harmonic (SH) photon energy of 75 meV less than the transition energy between the heavy hole (HH) ground state and conduction band (CB) ground state. The two fundamental photon energies were equal to half of the SH photon energy to calculate $\chi^{(2)}$ for second harmonic generation (SHG). Line broadening, Γ, was assumed to be 5 meV. In Eq. (3), $r_{e,hh}$ is the interband matrix element of the Bloch unit cell wavefunctions,

$$r_{e,hh} = \langle u_e^*|r|u_{hh}\rangle. \tag{4}$$

The first term within the summation of Eq. (3) is called the electron susceptibility, and the second, negative term is called the hole susceptibility as they contain the intersubband matrix elements of the electrons and holes, respectively,[15]

$$\chi_{xzx,e}^{(2)}(\omega_1, \omega_2) = \frac{N_z e^3 r_{e,hh}^2}{6\epsilon_0 \hbar^2} \sum_{k_\parallel} \sum_{m,n} \sum_l \frac{\langle \psi_{hhm}|\psi_{en}\rangle \langle \psi_{en}|z|\psi_{el}\rangle \langle \psi_{el}|\psi_{hhm}\rangle}{\left(\omega_{hhm}^{en}(k_\parallel) - \omega_1 - \omega_2 + i\Gamma\right)\left(\omega_{hhm}^{el}(k_\parallel) - \omega_1 + i\Gamma\right)}, \tag{5}$$

$$\chi_{xzx,hh}^{(2)}(\omega_1, \omega_2) = \frac{N_z e^3 r_{e,hh}^2}{6\epsilon_0 \hbar^2} \sum_{k_\parallel} \sum_{m,n} \sum_l \left(-\frac{\langle \psi_{en}|\psi_{hhm}\rangle \langle \psi_{hhm}|z|\psi_{hhl}\rangle \langle \psi_{hhl}|\psi_{en}\rangle}{\left(\omega_{hhm}^{en}(k_\parallel) - \omega_1 - \omega_2 + i\Gamma\right)\left(\omega_{hhl}^{en}(k_\parallel) - \omega_1 + i\Gamma\right)} \right), \tag{6}$$

$$\chi^{(2)}_{xzx}(\omega_1, \omega_2) = \chi^{(2)}_{xzx,e} + \chi^{(2)}_{xzx,hh}. \tag{7}$$

Henceforth, $\chi^{(2)}_{xzx}$ is referred to as $\chi^{(2)}$. Using the coupled QW structure, the wavefunctions and energy levels can be tailored to optimize the matrix elements and transition energies to achieve enhancement at wavelengths of interest.

A pair of asymmetric coupled GaAs QWs in AlGaAs was used as a prototype material system and structure for $\chi^{(2)}$ calculations, as depicted in Fig. 1. The QW asymmetry is defined by the asymmetry parameter $s = \frac{d_1 - d_2}{d_1 + d_2}$, where d_1 and d_2 are the thicknesses of QWs 1 and 2, respectively. We chose the AlGaAs material system as a prototype for its transparency to the fundamental and SH wavelengths and the favorable GaAs bandgap for SHG at S-, C-, L-, and U-band optical communications wavelengths. Furthermore, the optical and material properties are well known for developing the simulations, and high-quality epitaxial growth of GaAs/AlGaAs is well-established. In this work, the total QW thickness ($QW_{tot} = d_1 + d_2$) was varied between 5 and 12.5 nm, and the barrier thickness was fixed at 1 nm.

A Schrödinger–Poisson solver was used to determine the CB and HH energy levels and associated envelope wavefunctions.[19] The interband and intersubband transition dipole matrix elements were calculated from the associated wavefunctions. The interband matrix element of the unit cell wavefunctions was determined to be $r_{e,hh} = 7.51$ Å using density functional theory (DFT) performed with the Vienna *Ab initio* Simulation Package using HSE06 hybrid functionals. The summation over $k_{||}$ was converted to an integral in two-dimensional k-space (k_x, k_y). We found the integral over k states for $\chi^{(2)}$ saturated by one-tenth of the Brillouin zone from zone center ($k = 0$). Limiting the integration to one-tenth of the Brillouin zone from zone-center enabled employing the effective mass approximation without introducing significant error.

Previous studies of interband second-order optical nonlinearities used the tight-binding approach to find the wavefunctions and energy levels of the coupled QWs from those of the individual wells.[15] However, these methods do not fully capture the behavior of HH states, and how they localize into the individual wells at smaller asymmetries than CB states. This is due to the large effective mass of heavy holes. Furthermore, tight-binding methods break down at high asymmetries when one QW becomes very thin. As a result, previous theoretical predictions of interband nonlinear enhancement were weaker than theoretical and experimental intersubband enhancement results from around the same time. We have found that substantial enhancements of interband $\chi^{(2)}$ are predicted using rigorous wavefunction calculation techniques and considering all possible sets of transitions contributing to second harmonic generation.

To compare the quantum calculation methods, $\chi^{(2)}$ vs asymmetry for various total QW thicknesses was calculated for GaAs/AlGaAs asymmetric coupled QWs, as shown in Fig. 2. The wavefunctions and energy levels of the first two bound electron and heavy hole states were calculated using linear combination of atomic orbitals (LCAO) and Schrödinger–Poisson methods.

Employing energy levels and wavefunctions from Schrödinger–Poisson methods resulted in an order of magnitude larger $\chi^{(2)}$ than those predicted using LCAO methods. The rigorous quantum calculation methods are also valid across the full range of QW asymmetries, whereas the LCAO methods break down at high asymmetries. The results of Fig. 2 predict that the magnitude of $\chi^{(2)}$ increases with increasing total QW thickness, which is due to the
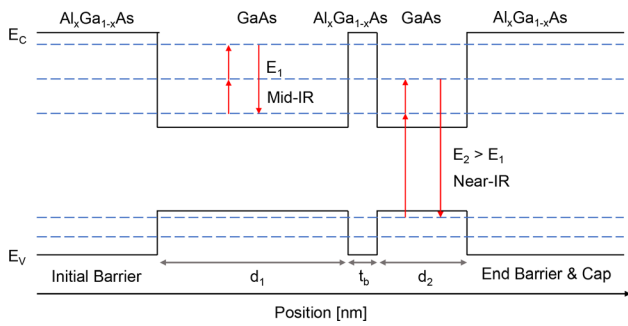

FIG. 1. Diagram detailing the GaAs/AlGaAs asymmetric coupled QW structure with intersubband and interband sum-frequency generation processes illustrated by arrows between the energy levels.
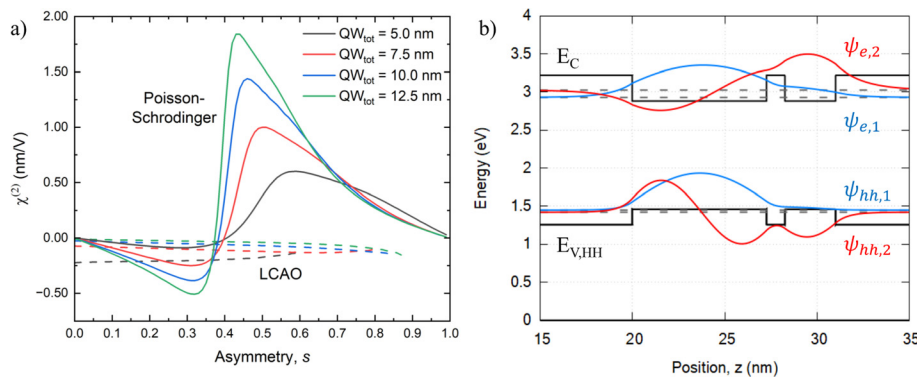

FIG. 2. (a) $\chi^{(2)}$ vs asymmetry for total QW thicknesses of 5, 7.5, 10, and 12.5 nm. The solid curves are results using rigorous Schrödinger–Poisson methods, and the dashed curves are results using the LCAO theory to generate wavefunctions and energy levels. The dashed curves are truncated at the asymmetries at which the LCAO theory begins to break down. The rigorous quantum calculation methods predict a full order of magnitude stronger $|\chi^{(2)}|$. (b) Wavefunctions using Schrödinger–Poisson methods of the first two bound states (blue and red, respectively) of the heavy hole and conduction bands for GaAs/Al$_{0.4}$Ga$_{0.6}$As asymmetric coupled quantum wells with $s = 0.45$.

increased strength of the dipole-like intersubband matrix element term. This trend of increasing $\chi^{(2)}$ with total QW thickness is not expected to hold for arbitrary thick QWs, since increasing the QW thickness also decreases the energy separations between the bound states in the conduction band and heavy hole band, which takes the photon energies further away from resonance. The peak $|\chi^{(2)}|$ predicted from Schrödinger–Poisson methods is 1.80 nm/V for the 12.5 nm total QW thickness structure, which is 10 times larger than the bulk $\chi^{(2)}$ of GaAs (185 pm/V).[20–22]

When calculating $\chi^{(2)}$, it is important to consider all possible sets of transitions between states as indexed by [m,n,l] in the summations in Eq. (3). Each transition set represents a possible pathway for the virtual population of electron–hole pairs with energy at the second harmonic of the fundamental photons. To show the contribution to $\chi^{(2)}$ from each set of transitions between states, $\chi^{(2)}$ was calculated for GaAs/Al$_{0.4}$Ga$_{0.6}$As coupled QWs with a total QW thickness of 10 nm and for QW asymmetries ranging from $s = 0.00$ to $s = 0.99$. Figure 3 shows the $\chi^{(2)}$ contribution from each [m,n,l] transition set with dashed lines and the total $\chi^{(2)}$ with the solid line.

In Fig. 3, the $\chi^{(2)}$ vs asymmetry curve for each transition set and the total $\chi^{(2)}$ curve all have $\chi^{(2)} = 0$ nm/V for $s = 0$ and $s = 0.99$. These correspond to symmetric structures where the two wells are the same thickness ($s = 0$), and where the second well is so thin, there is effectively one QW ($s = 0.99$). The contributions mostly pairwise cancel with each other, except for the [m,n,l] = [1,1,1] and [2,2,2] sets. This pairwise cancelation is shown in Fig. 4, with insets showing the corresponding states and transitions used in the matrix elements in Eqs. (5) and (6).

Aside from the [1,1,1] and [2,2,2] sets, the other pairs of contributions almost completely cancel one another. The [1,1,1] and [2,2,2] sets correspond to dipoles since both the conduction and hole susceptibility terms in each of those transition sets have a diagonal intersubband matrix element. In analyzing the wavefunctions, we found that the peak at low asymmetries ($s \sim 0.07$) in all the contributions was due to localization of the HH ground state and excited state into the wide well and thin well, respectively, while the CB states remained delocalized with significant wavefunction amplitude in both wells. The peak
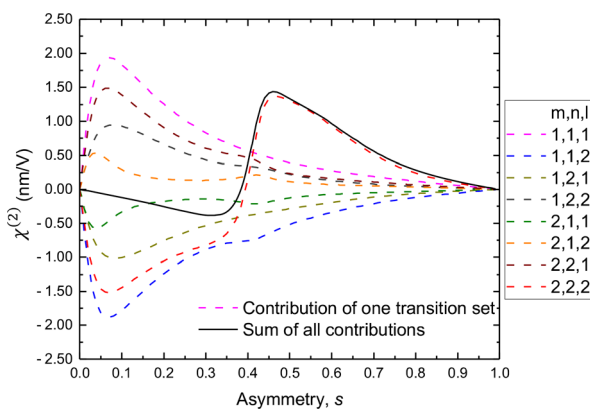
FIG. 3. Predicted $\chi^{(2)}$ for GaAs/Al$_{0.4}$Ga$_{0.6}$As asymmetric coupled QWs with a total QW thickness of 10 nm and 1 nm barrier thickness. The asymmetry, s, of the QWs is swept from $s = 0$ to $s = 0.99$. The dashed lines are $\chi^{(2)}$ calculated for individual sets of transitions, which are indexed as [m,n,l] in accordance with Eq. (1). The solid line is the total $\chi^{(2)}$.
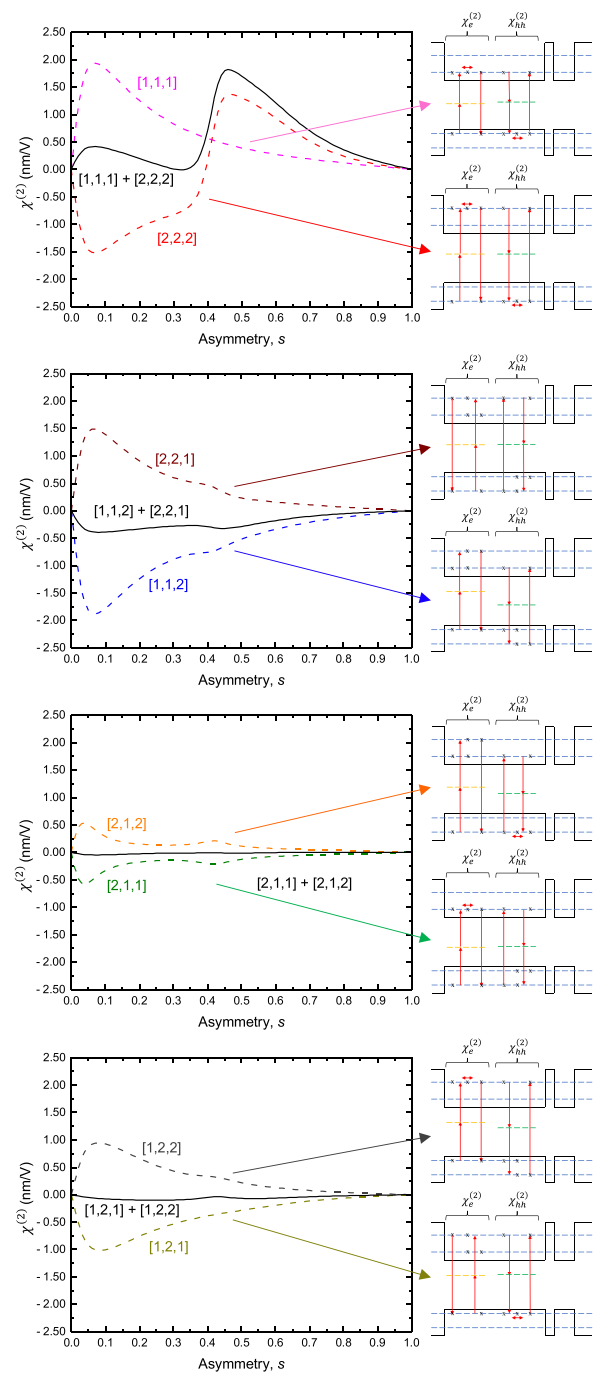
FIG. 4. Pairwise partial cancelation of the contributions to $\chi^{(2)}$ from the possible sets of transitions between two bound electron and two bound heavy hole states. In each plot, the two dashed lines are the predicted $\chi^{(2)}$ vs asymmetry calculated for individual transition sets, and the solid line is their sum. The band diagrams show which states are used for the SHG process for those transition sets. The "x" marks the states, the vertical arrows depict the two fundamental photons and one SH photon, the horizontal arrows signify a diagonal intersubband matrix element, and $\chi_e^{(2)}$ and $\chi_{hh}^{(2)}$ refer to the electron and hole susceptibilities defined in Eqs. (5) and (6), respectively.
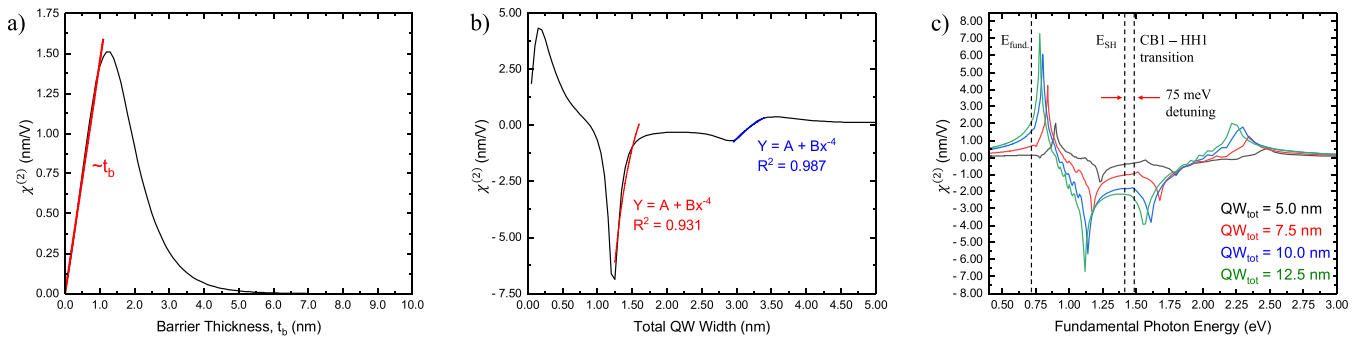
FIG. 5. (a) Dependence of $\chi^{(2)}$ on the thickness of the barrier between coupled GaAs/Al$_{0.4}$Ga$_{0.6}$As QWs with 10 nm total QW thickness and asymmetry $s = 0.45$. In the thin barrier regime ($t_b < 1.2$ nm), $|\chi^{(2)}|$ scales linearly with coupling barrier thickness. (b) Calculated $\chi^{(2)}$ for coupled GaAs/Al$_{0.4}$Ga$_{0.6}$As QWs with asymmetry $s = 0.45$ and barrier thickness $t_b = 1$ nm for total QW thicknesses ranging from 0 to 5 nm. Portions of the curve show the theoretically predicted inverse-fourth power dependence on total QW thickness. (c) Dependence of $\chi^{(2)}$ on the fundamental photon energy for coupled GaAs/Al$_{0.4}$Ga$_{0.6}$As QWs with asymmetry $s = 0.45$, barrier thickness $t_b = 1$ nm, and total QW thicknesses of 5, 7.5, 10, and 12.5 nm. The 75 meV detuned second harmonic photon energy (E$_{SH}$), the corresponding fundamental photon energy (E$_{fund.}$), and the conduction band ground state to heavy hole ground state transition energy are marked by dashed lines.

around 45% asymmetry in all the contributions was driven by the localization of the CB states to the individual wells. Simultaneously around 45% asymmetry, the HH excited state shifted to being confined in the wider well, while the CB excited state remained mostly confined in the thin well. This caused the sign change in the contribution to $\chi^{(2)}$ from the [2,2,2] transition set, which led to the incomplete cancelation with the [1,1,1] set and the resulting $\chi^{(2)}$ peak. These features of the [2,2,2] contribution to $\chi^{(2)}$ come from a breakdown of the tight-binding picture, which is why they were not observed in earlier work. The [1,1,2] and [2,2,1] transition sets represent SHG processes, where the two fundamental photons produce an interband and an intersubband virtual transition, and interband transition for the SH photon. For the [1,2,1], [1,2,2] and [2,1,1], [2,1,2] pairs, only the value of the l index changes. This results in a mix of SHG-like and dipole-like terms for the electron and hole susceptibilities. Overall, the total $\chi^{(2)}$ vs asymmetry curve is dictated by the [1,1,1] and [2,2,2] pair, which produces the small peak at $s = 0.35$ and the large peak at $s = 0.45$.

The thickness of the coupling barrier is an important component of the asymmetric structure. Without a sufficiently thick barrier, the structure is effectively one large well. $\chi^{(2)}$ reduces sharply as the coupling barrier thickness is increased beyond the optimal. With increasing coupling barrier thickness, the loss of QW asymmetry and the reduced matrix elements result in decreased $\chi^{(2)}$. To find the optimal thickness, $\chi^{(2)}$ was calculated for coupling barrier thicknesses ranging from $t_b = 0$ nm to $t_b = 10$ nm in GaAs/Al$_{0.4}$Ga$_{0.6}$As asymmetric coupled quantum wells with 10 nm total QW thickness and asymmetry $s = 0.45$. Previous work by Khurgin predicted that in the thin barrier regime, $\chi^{(2)}$ should scale linearly with the barrier thickness and inversely with the fourth power of the total QW thickness.[15] As shown in Fig. 5, for coupling barrier thicknesses less than 1.2 nm, we found that $\chi^{(2)}$ scales linearly with the coupling barrier thickness, but the relationship with total QW width was found to be more complicated. While the curve of $\chi^{(2)}$ vs total QW thickness shows the inverse-fourth power dependence over certain ranges, the overall curve presents a more complex structure, underscoring the importance of the rigorous quantum mechanical calculations employed here.

The interband $|\chi^{(2)}|$ is strongest when the resonance conditions are met, and the denominators of the susceptibility terms in Eq. (3) are

small. The largest predicted $|\chi^{(2)}|$ occurs when the second harmonic photon energy is resonant with the interband transition energy between the conduction band ground state and the heavy hole band ground state. This corresponds to the peak around 0.75 eV fundamental photon energy in Fig. 5(c). In this work, the photon energies were chosen such that the second harmonic photon energy was 75 meV detuned from the resonance. This approach avoids absorption of the fundamental photons, and the detuning was included to avoid absorption of the second harmonic photons. While the resonant, non-detuned second harmonic photon energy for maximum $|\chi^{(2)}|$ is above the bandgap and can be absorbed, many applications, such as metasurfaces, utilize normal incidence of thin structures, which are tolerant to moderate absorption. Since the photon energies are determined by the energy separation between the CB and HH ground states minus the desired detuning, the choice of photon energy is dependent on the structure design. This allows for coupled QW designs that can be tailored for the photon energy requirements of specific applications. It was predicted in Fig. 5(c) that the fundamental photon energy for peak $|\chi^{(2)}|$ increases as the total QW thickness is reduced due to the increased confinement.

This work suggests that interband second-order nonlinearities can be significantly enhanced by introducing structural asymmetry in the form of coupled QWs, well beyond earlier predictions. Rigorous quantum mechanical calculation methods and treatment of heavy hole states reveal the importance of dipole-like diagonal intersubband matrix element terms, resulting in predicted $\chi^{(2)}$ enhancements by a full order of magnitude compared to bulk GaAs. The optimal thickness of the wavefunction coupling barrier has also been determined. Overall, this work paves the way for designing epitaxially grown asymmetric layer structures with significantly enhanced second-order optical nonlinearity in the near infrared.

06 January 2024 18:07:03

AUTHOR DECLARATIONS
Conflict of Interest

The authors have no conflicts to disclose.

Author Contributions

Rithvik Ramesh: Conceptualization (equal); Data curation (equal); Formal analysis (equal); Investigation (equal); Methodology (equal); Project administration (equal); Software (equal); Visualization (equal); Writing – original draft (equal); Writing – review & editing (equal). **Seth R. Bank:** Conceptualization (equal); Formal analysis (equal); Funding acquisition (equal); Investigation (equal); Project administration (equal); Resources (equal); Supervision (equal); Writing – review & editing (equal). **Teddy Hsieh:** Conceptualization (equal); Formal analysis (equal); Investigation (equal); Methodology (equal); Software (equal). **Alec Mason Skipper:** Conceptualization (equal); Formal analysis (equal); Investigation (equal); Methodology (equal). **Qian Meng:** Formal analysis (equal); Investigation (equal); Methodology (equal); Software (equal). **Kevin C. Wen:** Formal analysis (equal); Investigation (supporting); Methodology (equal); Software (equal); Visualization (supporting). **Farbod Shafiei:** Formal analysis (supporting); Investigation (supporting). **Mark Wistey:** Formal analysis (supporting); Methodology (supporting); Supervision (equal); Writing – review & editing (equal). **Michael Downer:** Formal analysis (supporting); Methodology (supporting); Supervision (equal); Writing – review & editing (equal). **Jacob B. Khurgin:** Conceptualization (supporting); Formal analysis (supporting); Investigation (supporting); Methodology (supporting); Supervision (equal); Writing – review & editing (equal).

DATA AVAILABILITY

The data that support the findings of this study are available from the corresponding author upon reasonable request.

REFERENCES

[1] D. Kong, Y. Liu, Z. Ren, Y. Jung, C. Kim, Y. Chen, N. V. Wheeler, M. N. Petrovich, M. Pu, K. Yvind, M. Galili, L. K. Oxenløwe, D. J. Richardson, and H. Hu, "Super-broadband on-chip continuous spectral translation unlocking coherent optical communications beyond conventional telecom bands," Nat. Commun. **13**(1), 4139 (2022).

[2] D. Cotter, R. J. Manning, K. J. Blow, A. D. Ellis, A. E. Kelly, D. Nesset, I. D. Phillips, A. J. Poustie, and D. C. Rogers, "Nonlinear optics for high-speed digital information processing," Science **286**(5444), 1523–1528 (1999).

[3] D. E. Chang, V. Vuletić, and M. D. Lukin, "Quantum nonlinear optics— Photon by photon," Nat. Photonics **8**(9), 685–694 (2014).

[4] M. Stefszky, V. Ulvila, Z. Abdallah, C. Silberhorn, and M. Vainio, "Towards optical-frequency-comb generation in continuous-wave-pumped titanium-indiffused lithium-niobate waveguide resonators," Phys. Rev. A **98**(5), 053850 (2018).

[5] C. Wang, M. Zhang, X. Chen, M. Bertrand, A. Shams-Ansari, S. Chandrasekhar, P. Winzer, and M. Lončar, "Integrated lithium niobate electro-optic modulators operating at CMOS-compatible voltages," Nature **562**(7725), 101–104 (2018).

[6] N. Owschimikow, C. Gmachl, A. Belyanin, V. Kocharovsky, D. L. Sivco, R. Colombelli, F. Capasso, and A. Y. Cho, "Resonant second-order nonlinear optical processes in quantum cascade lasers," Phys. Rev. Lett. **90**(4), 043902 (2003).

[7] R. W. Boyd, *Nonlinear Optics*, 4th ed. (Academic Press, London, UK, 2020).

[8] L. Alloatti, C. Kieninger, A. Froelich, M. Lauermann, T. Frenzel, K. Köhnle, W. Freude, J. Leuthold, M. Wegener, and C. Koos, "Second-order nonlinear optical metamaterials: ABC-type nanolaminates," Appl. Phys. Lett. **107**(12), 121903 (2015).

[9] M. Zhang, B. Buscaino, C. Wang, A. Shams-Ansari, C. Reimer, R. Zhu, J. M. Kahn, and M. Lončar, "Broadband electro-optic frequency comb generation in a lithium niobate microring resonator," Nature **568**(7752), 373–377 (2019).

[10] S. J. Maddox, S. D. March, and S. R. Bank, "Broadly tunable AlInAsSb digital alloys grown on GaSb," Cryst. Growth Des. **16**(7), 3582–3586 (2016).

[11] N. D. Foster, A. K. Rockwell, J. A. McArthur, B. S. Mendoza, S. R. Bank, and M. C. Downer, "A study of second-order susceptibility in digital alloy-grown InAs/AlSb multiple quantum wells," Adv. Opt. Mater. **10**(15), 2102845 (2022).

[12] M. M. Fejer, S. J. B. Yoo, R. L. Byer, A. Harwit, and J. S. Harris, Jr, "Observation of extremely large quadratic susceptibility at 9.6–10.8 μm in electric-field-biased AlGaAs quantum wells," Phys. Rev. Lett. **62**(9), 1041–1044 (1989).

[13] C. Sirtori, F. Capasso, D. L. Sivco, S. N. G. Chu, and A. Y. Cho, "Observation of large second order susceptibility via intersubband transitions at $\lambda \sim 10$ μm in asymmetric coupled AlInAs/GaInAs quantum wells," Appl. Phys. Lett. **59**(18), 2302–2304 (1991).

[14] S. Scandolo, A. Baldereschi, and F. Capasso, "Interband near-infrared second-harmonic generation with very large $\|\chi^{(2)}(2\omega)\|$ in AlSb/GaSb-InAsSb/AlSb asymmetric quantum wells," Appl. Phys. Lett. **62**(24), 3138–3140 (1993).

[15] J. Khurgin, "Second-order nonlinear effects in asymmetric quantum-well structures," Phys. Rev. B **38**(6), 4056–4066 (1988).

[16] R. Atanasov, F. Bassani, and V. M. Agranovich, "Second-order nonlinear optical susceptibility of asymmetric quantum wells," Phys. Rev. B **50**(11), 7809–7819 (1994).

[17] N. Bloembergen, *Nonlinear Optics*, 4th ed. (World Scientific, Hackensack, NJ, 1996).

[18] J. Khurgin, "Second-order susceptibility of asymmetric coupled quantum well structures," Appl. Phys. Lett. **51**(25), 2100–2102 (1987).

[19] S. Birner, T. Zibold, T. Andlauer, T. Kubis, M. Sabathil, A. Trellakis, and P. Vogl, "nextnano: General purpose 3-D simulations," IEEE Trans. Electron Devices **54**(9), 2137–2142 (2007).

[20] M. M. Choy and R. L. Byer, "Accurate second-order susceptibility measurements of visible and infrared nonlinear crystals," Phys. Rev. B **14**(4), 1693–1706 (1976).

[21] R. L. Sutherland, *Handbook of Nonlinear Optics*, 2nd ed. (CRC Press, 2003).

[22] J. J. Wynne and N. Bloembergen, "Measurement of the lowest-order nonlinear susceptibility in III–V semiconductors by second-harmonic generation with a CO_2 laser," Phys. Rev. **188**(3), 1211–1220 (1969).